OPEN ACCESS
Article

Mechanical properties and failure mechanisms of loess in southern Xinjiang: insights from microstructural evolution

Xuanyu Gao, Wanli Xie*, Kangze Yuan and Gabriele Della Vecchia

***E-mail:** xiewanli@nwu.edu.cn

Received 10 April 2026; Revised 4 June 2026; Accepted 14 June 2026; Published 18 August 2026

https://doi.org/10.55092/cle20260010

Graphical Abstract

Part 1: Spatial microstructural gradients and mechanisms | Part 2: Macroscopic mechanics and microstructural evolution | Part 3: Relational evaluation between microscopic structure and mechanical properties

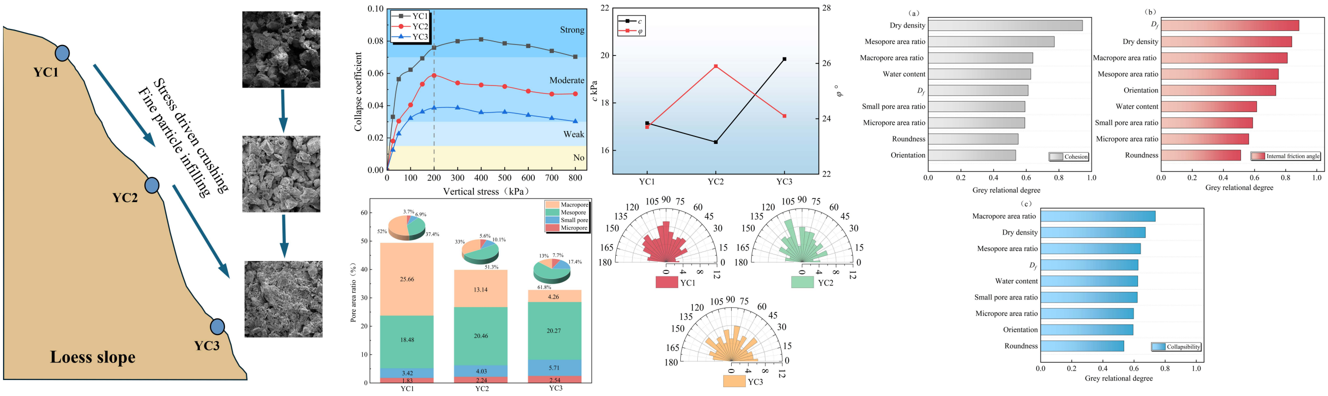

Highlights:

- Spatial heterogeneity in the mechanical properties of loess was quantified from the slope top to the toe.
- A loose, macropore-dominated skeleton progressively transforms into a dense, mesopore-dominated matrix downslope.
- Stress-induced particle crushing reduces the pore fractal dimension and weakens the preferential vertical orientation of pores.
- GRA reveals that distinct microstructural variables are associated with different macroscopic mechanical properties.

Mechanical properties and failure mechanisms of loess in southern Xinjiang: insights from microstructural evolution

Xuanyu Gao[1,2,3], Wanli Xie[1,2,3,*], Kangze Yuan[1,2,3], Gabriele Della Vecchia[4]

[1] State Key Laboratory of Continental Evolution and Early Life, Department of Geology, Northwest University, Xi'an, China

[2] Department of Geology, Northwest University, Xi'an, China

[3] Xi'an Key Laboratory of Prevention of Loess Dynamic Disaster and Restoration of Environment, Northwest University, Xi'an, China

[4] Department of Civil and Environmental Engineering, Politecnico Di Milano, Milan, Italy

***E-mail:** xiewanli@nwu.edu.cn.

Abstract: Elucidating the cross-scale coupling between microstructural evolution and mechanical behavior is crucial for understanding the progressive failure of loess slopes in arid regions. Focusing on a typical loess slope in the Yecheng region of southern Xinjiang, this study integrates oedometer-collapse tests, direct shear tests, scanning electron microscopy (SEM), and grey relational analysis (GRA) to quantitatively investigate the spatial heterogeneity of mechanical properties and microstructure. The results show that, from the slope top to the toe, the collapsibility coefficient decreases significantly from 0.076 to 0.039, whereas the shear-strength parameters exhibit nonlinear spatial variations. The internal friction angle initially increases and subsequently decreases, while cohesion shows a slight initial decrease followed by an increase to a peak value. At the microscale, variations in spatial position and overburden stress promote the transformation of an initially loose, point-contact skeleton dominated by macropores into a denser, matrix-supported structure dominated by mesopores and smaller pores. Concurrently, the preferential vertical orientation of the pores progressively weakens, while particle crushing and fine-particle infilling reduce morphological complexity, resulting in a decrease in the pore fractal dimension from 1.73 to 1.61. GRA further demonstrates that different macroscopic mechanical parameters are associated with distinct microstructural variables. Cohesion is strongly related to dry density, mesopore area ratio, macropore area ratio, and water content; the internal friction angle is most strongly associated with the pore fractal dimension; and collapsibility is predominantly related to the macropore area ratio and dry density. These findings establish quantitative links between microstructural evolution and macroscopic mechanical behavior and provide a physical basis for fine-scale landslide hazard assessment and geotechnical engineering design in arid loess regions.

Keywords: loess; microstructure; collapsibility; shear strength; grey relational analysis

1. Introduction

Loess is a loose aeolian deposit that formed primarily during the Pleistocene epoch of the Quaternary period. Predominantly composed of yellow silt, these deposits are typically distributed across arid and semi-arid regions, covering approximately 6% of the Earth's land surface (Haase *et al.* 2007; Li *et al.* 2020). In China, loess covers approximately 6.31×10^5 km², accounting for about 4.4% of the total land area. It is primarily distributed in northwestern China, encompassing Xinjiang, Gansu, Ningxia, Shaanxi, and Shanxi (Zhang *et al.* 2020). Typical aeolian loess is characterized by high porosity, loose packing, and a metastable structure (Gao 1988; Li *et al.* 2024). These properties make it highly susceptible to geohazards, leading to casualties, infrastructure damage, and farmland degradation, which severely threaten the local environment and economy. Statistically, approximately 30% of geohazards in China occur in loess regions annually, the majority of which are landslides (Zhang *et al.* 2010; Peng *et al.* 2015; Juang *et al.* 2019). Due to their high velocity, large volume, long runout distance, and strong impact force, landslides are among the most destructive geohazards in these regions. (Zhang et al. 2013; Zhuang et al. 2018). At low water contents, loess relies on its structural cohesion to resist slope failure. However, upon wetting, its mechanical properties deteriorate rapidly, ultimately triggering landslides. (Xu *et al.* 2018; Zhang *et al.* 2018; Lian *et al.* 2020). As macroscopic slope failures are mostly driven by progressive microstructural degradation, it is essential to understand how the loess microstructure responds and evolves at different locations. Therefore, bridging the gap between microscopic structural evolution and macroscopic mechanical failure is the primary motivation of this study.

Yecheng County is located in southwestern Xinjiang, at the tectonic contact zone between the West Kunlun Orogenic Belt and the southern margin of the Tarim Craton. Regional tectonic uplift has driven deep fluvial incision, forming numerous high and steep loess slopes. (Zheng *et al.* 2003).To clarify the hazard mechanisms of loess slopes and mitigate these landslide risks, extensive research has been conducted on loess landslides. On a regional scale, numerous studies have established relationships between slope environmental parameters and landslide occurrence to identify highly susceptible areas (Geertsema *et al.* 2009; Bièvre *et al.* 2018; Süzen *et al.* 2012; Zhuang *et al.* 2015). These evaluated parameters typically encompass geomorphology, precipitation, geological features, slope profiles, and vegetation cover. Furthermore, ring shear and triaxial tests are widely used to investigate the mechanisms and conditions of soil failure (Vithana *et al.* 2011; Li *et al.* 2013; Fan *et al.* 2017; Wang *et al.* 2019;Zhou *et al.* 2023). These laboratory tests at the mesoscale reveal that environmental perturbations, including variations in water content, capillary forces, matric suction, and salt migration, significantly weaken soil cohesion and alter the internal friction angle. However, macroscopic characteristics are largely determined by their microstructure (Nan *et al.* 2021; Lv *et al.* 2024; Wang *et al.* 2025b;. Therefore, linking microstructural evolution to macroscopic mechanical properties is essential for fully understanding loess instability. In recent years, considerable progress has been made in understanding the evolution of loess microstructures. By utilizing advanced imaging and quantitative techniques, researchers have extensively investigated the microscopic mechanisms of loess degradation under complex hydro-mechanical coupling (Qin *et al.* 2024; Wang *et al.* 2025a). Despite these micro-scale advancements, applying these findings to complex slope systems reveals significant gaps (Li *et al.* 2019; Wei *et al.* 2020; Wang *et al.* 2022). Current studies largely treat the slope as a homogeneous material, neglecting how mechanical properties evolve across different slope positions. Furthermore, quantitatively linking these microstructural changes to the evolution of macroscopic mechanical behavior remains a challenge. The soil is governed by multiple interacting feature variables and a single microstructural parameter may influence multiple mechanical properties and is strongly correlated with other physical state parameters. Traditional statistical methods often struggle to process this partially known and highly correlated information matrix, failing to identify the key factors driving microstructural evolution (Yuan *et al.* 2022; Nie *et al.* 2023; Ye *et al.* 2024). Therefore, there is an emerging need to introduce new methods to systematically elucidate the relationship between the mechanical behavior of loess and its microstructural evolution. Grey relational analysis (GRA), as an effective mathematical tool for handling small samples, multiple variables, and nonlinearities, provides an ideal approach for revealing this cross-scale response mechanism (Liu *et al.* 2022; Chakraborty *et al.* 2023; Motameni *et al.* 2025). Compared with previous studies, this research places particular emphasis on the quantitative characterization of loess microstructural evolution and its linkage with macroscopic mechanical behavior. By integrating scanning electron microscope (SEM) image analysis with GRA, this study aims to identify the relative contributions of different microstructural parameters to the shear strength and collapsibility of loess, thereby providing a quantitative perspective on the micro–macro relationship governing slope stability.

Based on the above discussion, this study focuses on the loess slopes in Yecheng County, southwestern Xinjiang. Firstly, oedometer-collapse tests and direct shear tests were carried out on original loess samples collected from different spatial locations (slope top, middle, and toe). Subsequently, the microstructural evolution was analyzed using SEM images, and the geometric characteristics of the pores were quantitatively extracted using Avizo software. Finally, the GRA model was introduced to systematically quantify the coupling relationships between macroscopic mechanical degradation and microscopic structural variables. By bridging the macroscopic behaviors and microscopic structure of loess, this study provides a comprehensive understanding of the progressive failure mechanisms of loess slopes, ultimately offering a solid physical basis for fine-scale hazard evaluation and sustainable geotechnical engineering in arid regions.

2. Material and methodology

2.1. Study area

The study area is located in Yecheng county, Xinjiang, China, in the interior of the Eurasian continent and far from the sea (Figure 1). The region experiences a typical continental arid climate, with a mean annual precipitation of approximately 55 mm, most of which falls between April and July. Geomorphologically, the landscape is dominated by piedmont proluvial fans, proluvial–aeolian aprons, and landslide deposits. The stratigraphic sequence mainly consists of Upper Pleistocene (Q_3) loess, with thickness around 3–5 m. Due to its metastable structure and high porosity, the loess is extremely sensitive to water infiltration induced by heavy rainfall or irrigation, which may lead to a sharp reduction in strength and trigger collapse and instability. Consequently, this area is among the most landslide-prone zones in the Chinese loess region.

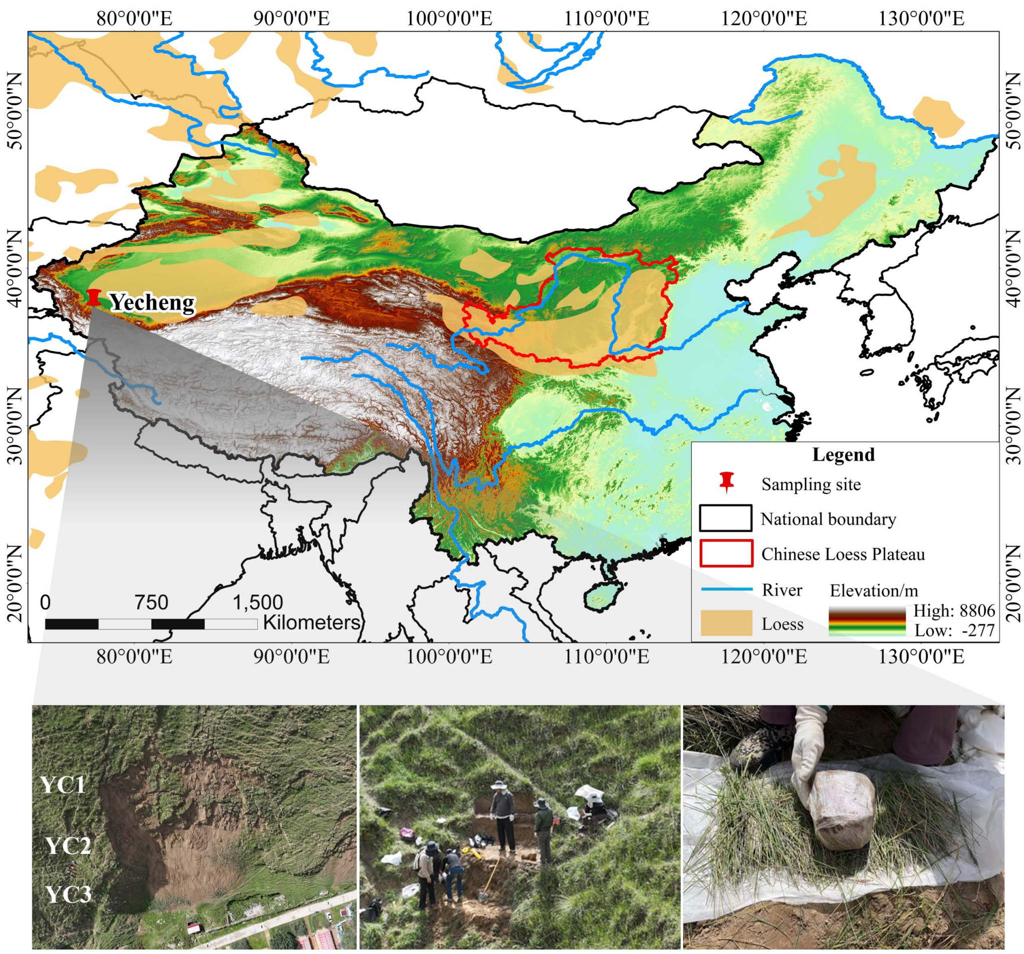

Figure 1. Spatial distribution of loess in China and the location of the sampling site.

2.2. Test materials

To investigate the engineering properties and original structural characteristics of the loess in different sections of the study area, sampling was carried out on the same slope, with samples collected from three distinct sections: YC1, YC2 and YC3. Sampling locations were selected to avoid areas of disturbance, ensuring that the samples accurately reflect the original structure and properties of the loess. Multiple layers of protection were employed to prevent disturbance to the samples during transport. After arriving, the physical properties of the loess were determined in accordance with the Standard for Geotechnical Testing Method (Ministry of Housing and Urban-Rural Development of the People's Republic of China 2019), as in Table 1.

Table 1. Physical properties of loess.

Sample	Dry density (g/cm^3)	Natural water content (%)	Specific gravity	Plastic limit (w_P/%)	Liquid limit (w_L/%)
YC1	1.15	14.3	2.71	17.9	29.3
YC2	1.22	7.9	2.71	17.6	29.0
YC3	1.31	15.6	2.71	18.0	29.7

2.3. Direct shear test

The direct shear test is widely applied to assess the shear properties of soils, due to its simplicity and rapid access to shear strength parameters. Samples were prepared in a cylindrical shear box measuring 61.8 mm in diameter and 20 mm in height (Figure 2). To investigate the shear behavior under field conditions, the specimens were tested at their original water content without pre-saturation. The shear process was carried out in accordance with the GB/T 50123 standard under unconsolidated-undrained conditions. The samples were sequentially tested under vertical pressures of 50, 100, 150, and 200 kPa at a shear rate of 0.8 mm/min. This quick-shear rate was specifically adopted to simulate the rapid sliding phase of loess landslides, during which the localized sliding zone undergoes instantaneous, undrained shearing without sufficient time for stress relaxation or moisture redistribution. Each test was repeated three times to ensure the reproducibility of the results.

2.4. Oedometer-collapse test

To quantitatively assess the collapsibility characteristics of the loess in the study area, a series of double-line oedometer tests were conducted in accordance with the GB/T 50123 standard. Two parallel specimens from each sampling location were tested under different hydraulic conditions: one at its natural moisture content and the other being saturated at a specific vertical stress level. All samples were subjected to increasing vertical pressure of 50 kPa, 100 kPa, 200 kPa, 300 kPa, 400 kPa and 800 kPa (Figure 2). After reaching the desired stress level and after equilibration of pore pressure, water was added to the instrument from top to bottom and vertical displacement was measured. When the collapse deformation rate was less than 0.01 mm/h, the final displacement was recorded. The collapse coefficient (δ_s) was calculated using the following equation:

$$\delta_s = \frac{h_0 - h'_p}{h_0} \quad (1)$$

where h_0 represents the initial height of the sample at the relevant stress level and where h'_p represents the height of the inundated sample at a certain vertical stress level after stabilization of the vertical displacement.

2.5. SEM test

2.5.1. Acquisition of microstructural images

To explore the microstructural characteristics and evolution of the loess in the study area, samples were observed using the FEI Quanta 450 FEG SEM. To preserve the original microstructure of the loess and prevent shrinkage cracks caused by conventional oven drying, the samples were air-dried (Xiao *et al.* 2022a). Subsequently, the samples were gently snapped to expose fresh cross-sections, ensuring that undisturbed internal structures were observed. To enhance conductivity, the observation surfaces were coated with gold via sputtering. The SEM was operated at an acceleration voltage of 10 kV with a working distance of approximately 20 mm. During the SEM observation, a wide range of magnifications from 100× to 3000× was employed to simultaneously capture both the overall particle arrangement and local inter-particle contact features. However, for the subsequent quantitative extraction using Avizo software, images specifically at 800× magnification were uniformly selected as the standard. At this specific scale, the field of view is sufficiently large to ensure the statistical representativeness of the pore and grain distribution, while the resolution remains high enough to accurately delineate the complex boundaries of microscopic features for quantitative segmentation.

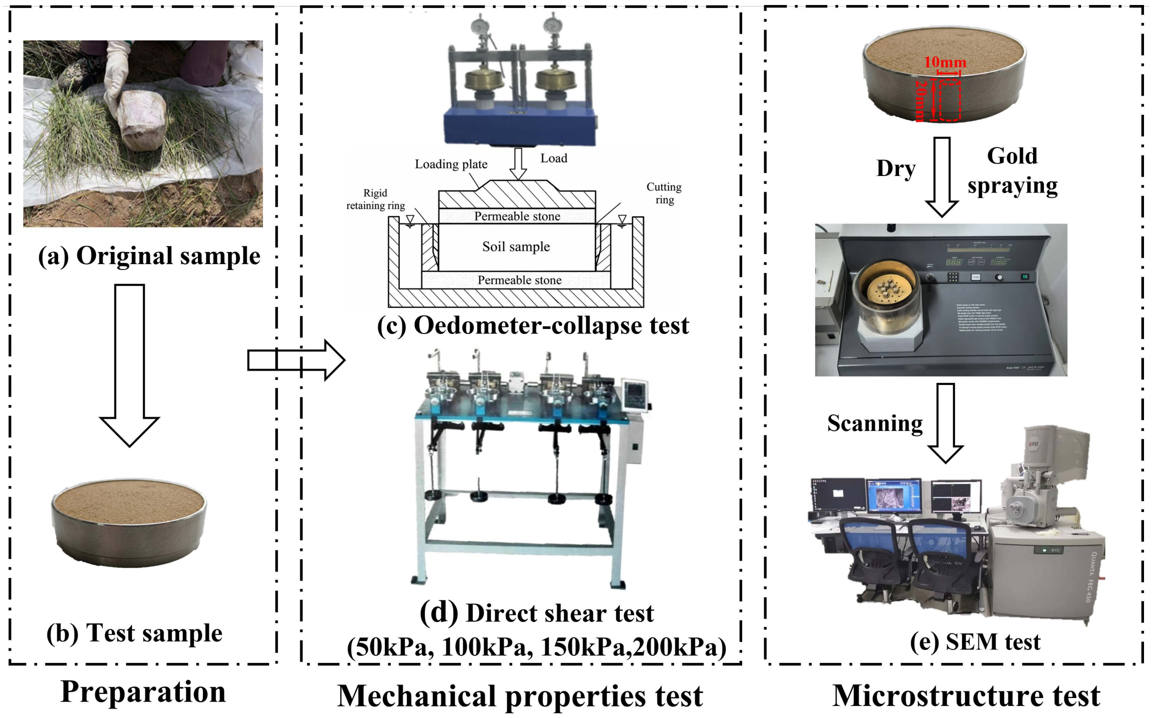

Figure 2. Workflow of the mechanical property tests and microscopic tests.

2.5.2. Image processing

Image processing is an indispensable step in the quantitative study of the evolution of microstructural features within loess at different depths. To obtain microstructural information of the sample, Avizo software was used to process the SEM images at 800× magnification. The specific processing workflow is as follows: the original image is processed using a non-local means filter to reduce background noise while preserving edge sharpness. Subsequently, a global thresholding method is employed to separate the image into soil bulk and pore space (Figure 3). After image processing, several microstructural parameters were extracted from the images using the Avizo software for further analysis. These parameters included pore area, perimeter, orientation and equivalent diameter *d*. Furthermore, pore roundness and fractal dimension (D_f) were introduced to further quantify the distribution of pore shapes. In addition, according to the loess pore classification system proposed by (Lei 1988), pores in loess samples were classified into four types based on their diameter: micropores (*d* = 0 to 2 µm), small pores (*d* = 2 to 8 µm), mesopores (*d* = 8 to 32 µm), and macropores (*d* > 32 µm).

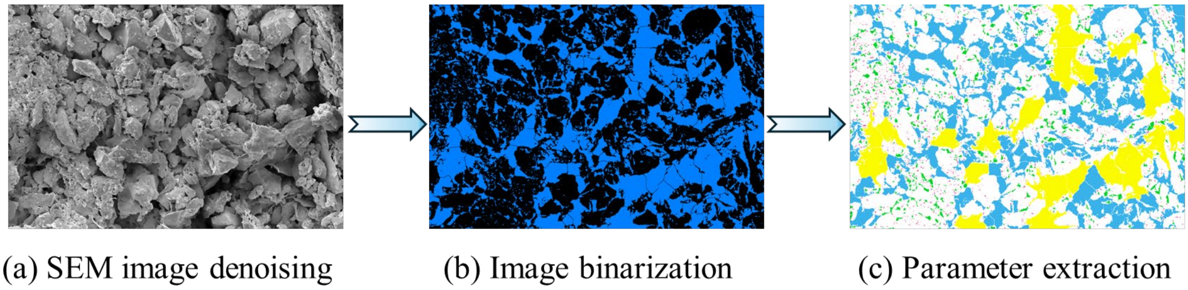

Figure 3. Steps applied for the SEM images quantitative interpretation.

2.6. Grey relational analysis

The mechanical properties of loess (e.g., cohesion *c*, internal friction angle *φ*, and collapsibility coefficient *δs*) are influenced by its microstructure and state parameters. Due to the high nonlinearity and complexity of the soil system, coupled with the multiplicity of feature variables, traditional statistical methods struggle to accurately quantify the coupling relationships among these factors. GRA, a core component of Grey System Theory, can effectively handle "small dataset with limited information" systems characterized by partially known and partially unknown information (Xiao *et al.* 2012; Liu *et al.* 2013). This method measures how closely related different sequences of data are, distinguishing between dependent variables (the reference sequence) and independent variables (the comparative sequences). We utilized this approach to systematically analyze the relationships between the physical state of loess and its mechanical behavior. Specifically, cohesion *c*, internal friction angle *φ*, and collapsibility coefficient δ_s were individually designated as the dependent variables. Meanwhile, a total of 9 parameters were defined as the independent variables, including dry density (ρ_d), water content (*ω*), pore orientation (*O*), pore fractal dimension (D_f), pore roundness (*R*), and the area ratios of different pore sizes (micropore, small pore, mesopore, and macropore). It should be noted that some microstructural parameters may exhibit inherent interdependence. However, unlike regression-based approaches, GRA evaluates the geometric similarity between normalized sequences rather than estimating independent regression coefficients, thereby remaining highly robust against multicollinearity among the comparison variables. The specific calculation procedures are as follows:

2.6.1. Designation of reference and comparison sequences

Firstly, the reference sequence and the comparative sequences should be defined. Let the reference sequence of the system be denoted as $X_0 = \{x_0(k), k = 1,2, \dots, n\}$, where *k* represents the sample index and *n* the number of measured data points. Similarly, let the sequence of feature parameters to be compared be $X_i = \{x_i(k), k = 1,2, \dots, n\}$.

2.6.2. Data dimensionless processing

Given the significant differences in physical dimensions and orders of magnitude among the various parameters (e.g., dry density and micropore area ratio), the raw data are normalized to eliminate the adverse effects of dimensionality on the calculation results. Therefore, mean normalization was applied to the original dataset. The transformation formula is expressed as follows and it has been applied to each reference and feature parameter:

$$x_i^*(k) = \frac{x_i(k)}{\frac{1}{n}\sum_{k=1}^{n} x_i(k)} \tag{2}$$

$$x_0^*(k) = \frac{x_0(k)}{\frac{1}{n}\sum_{k=1}^{n} x_0(k)} \tag{3}$$

where $x_i^*(k)$ and $x_0^*(k)$ represent the dimensionless comparison sequence and the reference sequence.

2.6.3. Calculation of grey relational coefficient

The absolute difference $\triangle_i(k) = |x_0^*(k) - x_i^*(k)|$ between the reference sequence and each comparison sequence at each data point is calculated. Subsequently, the maximum difference $\triangle_{max}$ and minimum difference $\triangle_{min}$ over all data points are identified. The grey relational coefficient $\xi_i(k)$ is then calculated using the following equation:

$$\xi_i(k) = \frac{\triangle_{min} + \rho\,\triangle_{max}}{\triangle_i(k) + \rho\,\triangle_{max}} \tag{4}$$

where ρ is the distinguishing coefficient, introduced to attenuate the distorting effect of extreme values on the calculation results, generally taken equal to 0.5 (Kuo *et al.* 2008).

2.6.4. Calculation of grey relational degree

While relational coefficients capture point-by-point correlations, these individual values must be aggregated to assess the overall relationship between the sequences. To systematically evaluate the correlation between two sequences, the average value of the relational coefficients is calculated to obtain the Grey Relational Degree (γ_i). The calculation equation is as follows:

$$\gamma_i = \frac{1}{n}\sum_{k=1}^{n} \xi_i(k) \tag{5}$$

The value of g_i degree ranges from 0 to 1. A value closer to 1 indicates that the corresponding feature parameter exerts a more significant controlling effect on the evolution of the reference sequence. Conversely, a lower value implies a weaker influence.

3. Results and discussion

3.1. Mechanical properties of the original loess

3.1.1. Shear behavior

To investigate the mechanical triggering mechanisms of loess landslides in Yecheng, the shear behavior of undisturbed samples was evaluated. The results revealed significant spatial heterogeneity in the shear strength properties, reflecting the unique stress paths and mechanical degradation histories experienced at different locations (Figure 4). At the upper slope (YC1), the soil exhibits a relatively low internal friction angle (φ = 23.7°) and moderate cohesion (c =17.15 kPa). In contrast, the middle section (YC2) shows a slight reduction in cohesion to 16.35 kPa but a notable increase in the internal friction angle to 25.9°. This behavior suggests that the middle slope may have experienced more intense leaching or surface erosion. In addition, prolonged gravitational creep likely disrupted the original cementation of the loess, leading to a reduction in cohesion, while promoting particle rearrangement and enhanced interparticle friction. The shear strength in the toe (YC3) region increases significantly, with cohesion reaching 19.85 kPa and the internal friction angle at 24.1°. This critical region is subjected to substantial passive compressive stress exerted by the overlying mobilized mass. This intense stress concentration mechanically compresses the local sliding zone, enhancing its cohesive resistance and functioning as a terminal retaining block. Overall, this spatial variation in shear parameters is consistent with the mechanical evolution of loess landslides, as the upper section typically undergoes tensile failure first, the middle section experiences significant structural degradation, while the lower section is subject to stress concentration and compaction (Jia *et al.* 2025; Xie *et al.* 2021).

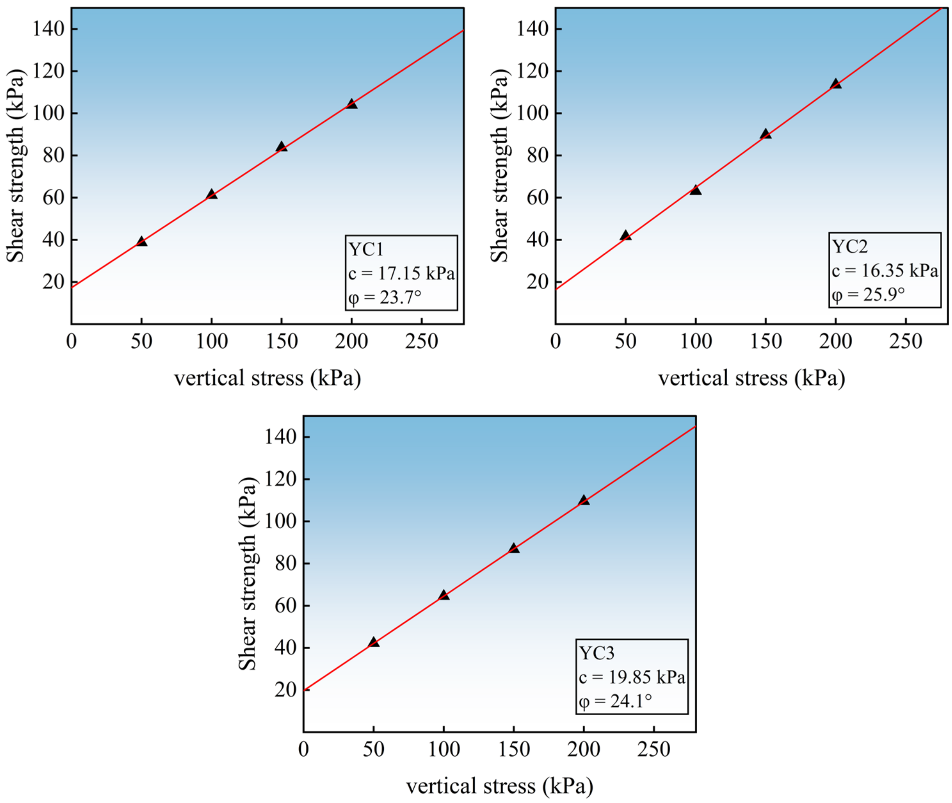

Figure 4. Shear strength envelopes.

3.1.2. Collapsibility of loess

The collapsibility of loess samples exhibits significant spatial heterogeneity and follows distinctly different patterns from the top to the toe of the slope (Figure 5). For all samples (YC1, YC2, and YC3), the curves of the collapse coefficient (δs) exhibit a maximum collapse, with the collapsibility index showing a pattern of rapid increase followed by a gradual decline as vertical stress increased. Notably, the peak collapsibility of all samples consistently concentrated within the 200 to 400 kPa. This range can be identified as a critical zone, within which the synergistic interaction between the role of matric suction and mechanical loading maximizes volumetric collapse. In accordance with the Chinese National Standard for building construction in collapsible loess regions (Ministry of Housing and Urban-Rural Development of the People's Republic of China 2018), the collapsibility coefficient of loess under a pressure of 200 kPa is employed as the standard for quantitatively evaluating its collapsibility in practical engineering. Based on this standard, the loess collapsibility is classified into four categories: non-collapsible ($\delta_s \leq 0.015$), weakly collapsible ($0.015 < \delta_s \leq 0.030$), moderately collapsible ($0.030 < \delta_s \leq 0.070$), strongly collapsible ($\delta_s > 0.070$). Table 2 presents the collapse coefficients of different samples under 200 kPa pressure. Specifically, the YC1 loess exhibits the highest collapsibility, with a δs value of 0.076, which can be classified as strongly collapsible. This indicates that the loess at the slope top possesses an abundant volume of large pores, which provides sufficient space for collapse to occur, making it highly susceptible to wetting-induced structural instability under natural conditions. As the sampling location moves down the slope, collapsibility shows a decreasing trend. YC2 ($\delta s = 0.059$) and YC3 ($\delta s = 0.039$) loess are classified as moderately collapsible. The pronounced differences among the YC1, YC2, and YC3 curves further highlight that even within the same loess slope, spatial variability in depositional structure leads to significant differences in mechanical behavior and failure risk.

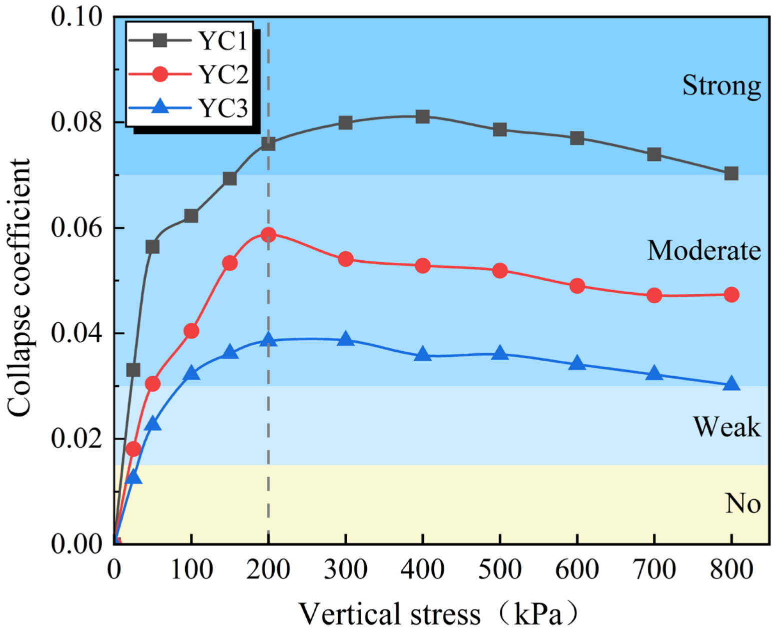

Figure 5. Evolution of the collapse coefficient with the applied vertical stress.

Table 2. Collapse coefficients of the loess at different depths at a vertical stress 200 kPa.

Sample	YC1	YC2	YC3
δ_s (200 kPa)	0.076	0.059	0.039
Collapse potential	Strong	Moderate	Moderate

3.2. Evolution of the microstructure of the original loess

3.2.1. Microstructure morphology

The qualitative assessment of soil microstructure generally relies on four interrelated elements: particles, contact relationships, pore forms, and the degree of cementation (Rabot *et al.* 2018; Tang *et al.* 2023). As shown in Figure 6, the particle composition of the loess in the study area consists primarily of silt and silt-clay aggregates. The microstructural contact modes exhibit significant spatial heterogeneity. Based on the contact area, the interactions between loess particles are primarily characterized by point and face contacts. Mechanically, point contacts result in unstable stress distribution, whereas face contacts promote a compact arrangement, enhancing the shear strength and structural integrity of loess. Observations indicate that the skeleton of sample YC1 is characterized by abundant point contacts. Conversely, in samples YC2 and YC3, point contacts are substantially reduced in favor of face contacts. This significant shift in contact patterns drives the structural evolution of the loess from a loose, metastable state toward a more compact and stable structure. Concurrently, the pore structure also has significant evolution. The pore system of loess exhibits a distinct dual structure, comprising inter-aggregate and intra-aggregate pores (Gao *et al.* 2026). Intra-aggregate pores, primarily developing within clay or silt-clay aggregates, are characterized by significantly smaller diameters compared to inter-aggregate pores, typically ranging from the micrometer to sub-micrometer scale (Li *et al.* 2022). The YC1 loess exhibits numerous interconnected macropores between particles, resulting in very high porosity. These macropores provide ample space for the occurrence of collapse, which also reduces overall stability and makes the loess highly susceptible to geological hazards under wet loading conditions. Transitioning from YC1 to YC2, the size and connectivity of these pores significantly decrease, indicating that initial compaction has occurred. In the YC3 loess, the pore dimensions are further compressed and the macropores are largely infilled by redistributed fine particles and cementitious materials. Consequently, the pore structure transforms into a dense matrix predominantly composed of fine, isolated micropores. Based on the degree of particle cementation, they can be classified into three states: weak, medium, and strong (Xu *et al.* 2023). In samples YC1 and YC2, the loess primarily exhibits a weak to medium degree of cementation. Morphologically, this is primarily characterized by faint film or point-contact cementation, interspersed with bridging cementation. In sample YC3, the degree of cementation is significantly enhanced, evolving into a dense and robust matrix-supported structure.

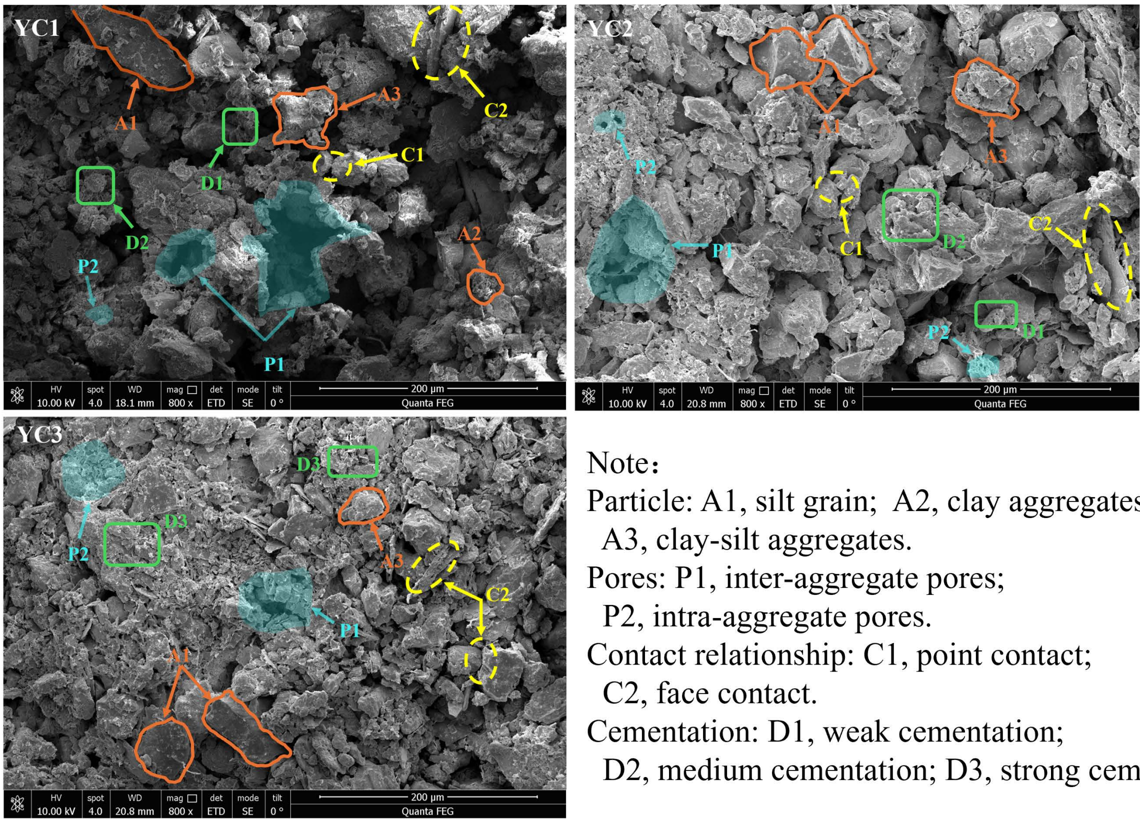

Note：
Particle: A1, silt grain; A2, clay aggregates; A3, clay-silt aggregates.
Pores: P1, inter-aggregate pores; P2, intra-aggregate pores.
Contact relationship: C1, point contact; C2, face contact.
Cementation: D1, weak cementation; D2, medium cementation; D3, strong cementation.

Figure 6. Microstructure morphology of the loess samples.

3.2.2. Pore area distribution

To characterize the pore distribution of different samples, Avizo software was employed to extract pore area distribution data. As illustrated in Figure 7, the microstructural pore distribution of the loess in the study area exhibits a distinct spatial gradient. From the top of the slope (YC1) to the toe (YC3), the total pore area ratio of the loess decreases significantly. Specifically, the evolution of macropores is the most pronounced. At YC1, macropores dominate the pore structure, accounting for 52% of the total pores with an area fraction of 25.66%. However, macropores decrease significantly toward the slope toe. The macropore ratio drops to 13.14% and 4.26% at YC2 and YC3, which consequently reduces its contribution to the total porosity to 33% and 13%, respectively. Conversely, the relative ratios of mesopores, small pores, and micropores exhibit an increasing trend. The ratio of mesopores to the total pore area rose from 37.4% at YC1 to 61.8% at YC3, making them the dominant pore type. Meanwhile, the contributions of small pores and micropores to the total pore area also increased from 6.9% and 3.7% to 17.4% and 7.7% respectively. This transition from a macropore-dominated structure at the slope top to a mesopore-dominated one at the slope toe is primarily driven by mechanical compaction. Increasing soil weight and stress downslope force larger macropores to collapse into smaller pores. Concurrently, rainfall washes fine particles down the slope. These particles accumulate at the slope toe, filling original macropores and further dividing them into smaller pores. This spatial reorganization of the pore structure fundamentally alters the mechanical properties of the slope.

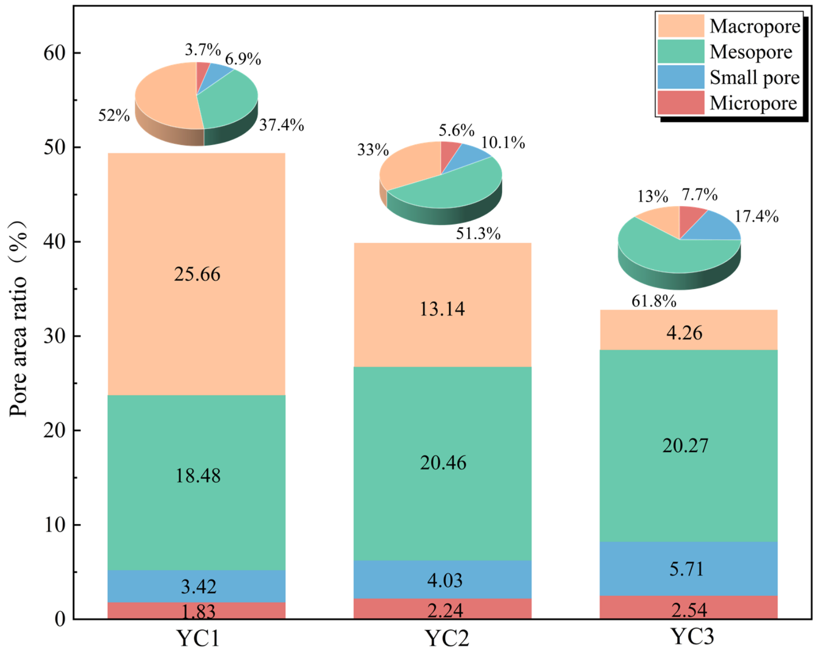

Figure 7. Changes in area distribution of the four loess pores types; the pie charts show the proportion of the total pore area represented by the four pores.

3.2.3. Pore orientation distribution

The pore orientation angle, defined as the angle of inclination of the major axis of a pore relative to the horizontal plane, serves as a key microscopic indicator for studying the pore structure of loess (Griffiths *et al.* 2017; Li *et al.* 2017). The pore orientation characteristics of the loess samples were quantitatively analyzed using rose diagrams, as illustrated in Figure 8. Moving down to YC2, the preferred vertical orientation begins to weaken. The major peaks shift, showing significant concentrations around 105° to 120°. At YC3, the dominance of vertical pores is significantly reduced, while the frequency of pores in low-angle and sub-horizontal ranges (e.g., 15° to 45° and 135° to 165°) notably increases. The spatial evolution of pore orientation from YC1 to YC3 provides crucial microscopic evidence for stress-induced structural degradation within loess slopes. Specifically, the loess at YC1 preserves its original structure, which is characterized by vertical macropores and root channels inherited from aeolian deposition. Consequently, its microstructure remains predominantly vertically oriented. However, moving towards YC3, the soil matrix experiences a complex stress state dominated by increasing overburden and gravity-driven shear stresses. Driven by persistent shear and potential slope creep, the primary vertical structural linkages gradually yield. Ultimately, this causes the highly aligned vertical pores to transform into a dispersed, horizontally inclined pore structure.

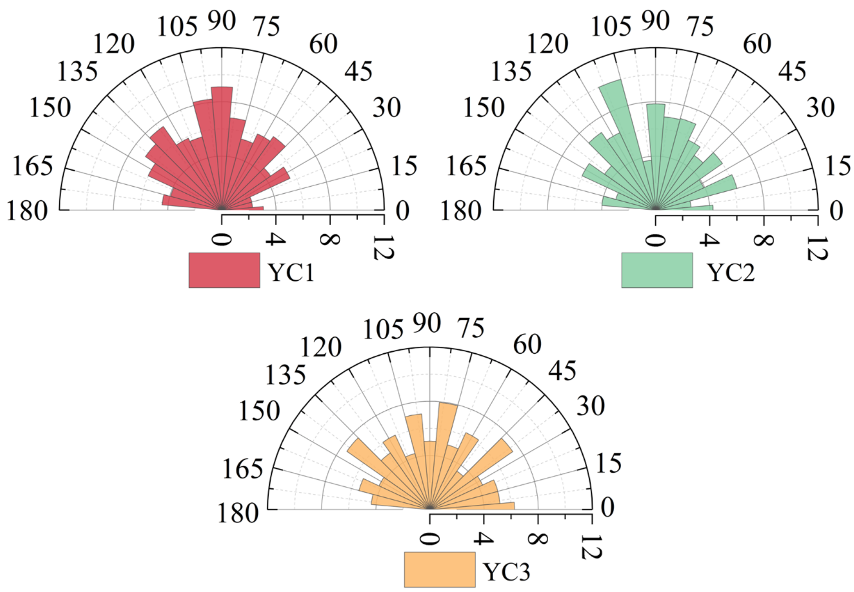

Figure 8. Pore orientation of loess samples.

3.2.4. Pore shape distribution

To quantitatively characterize the morphology of the pores, roundness (R) is introduced as a primary geometric shape descriptor in this study. The equation for calculating the roundness is as follows:

$$Roundness = \frac{4\pi A_{pore}}{P_{pore}^2} \quad (6)$$

where A_{pore} is the pore area and P_{pore} represents the pore perimeter. The roundness takes values ranging from 0 to 1. The closer the roundness is to 1, the closer the pore shape is to a circle. Figure 9 shows the relative and cumulative frequency distributions of the calculated pore roundness of three samples. In YC1, the relative frequency of pore roundness peaks in the extremely low roundness range of 0.05 to 0.1, accounting for 35% of the total pore. Moving to YC2, the morphological distribution begins to widen. The dominant peak of relative frequency shifts rightward to the 0.1 to 0.2 range, while the proportion of moderately rounded pores (0.3 to 0.5) increases significantly. At YC3, the primary peak shifts to the range of 0.2 to 0.3, accompanied by a significant increase in moderately rounded pores ($0.3 < R < 0.6$). This evolutionary process is highly consistent with the stress-induced densification mechanism discussed previously. Subjected to overburden pressure and localized shear stresses at the slope toe, the elongated macropores undergo compression, evolving into a more compact pore structure. Concurrently, the downward migration and subsequent infilling of fine particles into larger pores effectively smooth their angular boundaries.

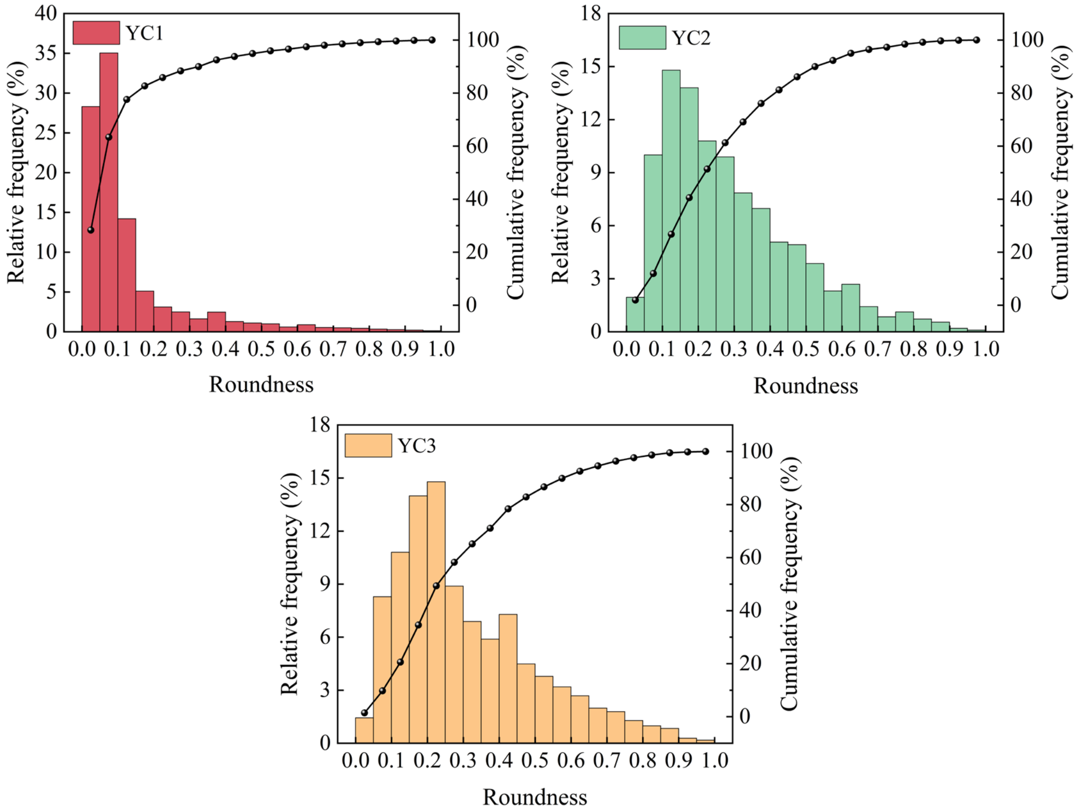

Figure 9. Distribution of pore morphology parameters in loess samples at different depths.

In addition, the fractal dimension (D_f) was introduced to quantitatively assess the complexity of pore morphology (Sun *et al.* 2018; Xiao *et al.* 2022b). It is worth noting that the D_f in this study is quantitatively extracted from binarized SEM images. Since the analysis focuses on the planar projection of the pore structure, the fractal dimension ranges from 1 to 2. The equation used is as follows:

$$\log P = \frac{1}{2} D_f * \log A + C \quad (7)$$

where A represents the pore area, P represents the perimeter of the pore, C is the fitting constant term, and a higher fractal dimension (D_f) indicates a more complex pore morphology.

Table 3 fractal dimension of the pores for different samples. presents the fractal dimensions for different samples. The fractal dimension of the pore structure exhibits a clear monotonically decreasing trend from the top to the toe of the slope, although the range of variation is relatively small, ranging from 1.73 to 1.61. The decrease in fractal dimension is driven by the synergistic effect of mechanical crushing and fine-particle infilling. At YC1, the primary pore structure of the loess is well-developed. Moving towards the slope toe, the increased overburden pressure and shear stress crush these irregular pores. Meanwhile, migrating fine particles fill the rough boundary depressions, effectively smoothing the pore outlines and thereby reducing the overall structural complexity.

Table 3. Fractal dimension of the pores for different samples.

Sample	YC1	YC2	YC3
D_f	1.73	1.68	1.61

3.3. Relational evaluation between microscopic structure and mechanical properties

To quantitatively reveal the underlying mechanisms driving the hydro-mechanical degradation of the loess slopes, GRA was employed to have an insight into the correlation between microscopic structural parameters and macroscopic mechanical properties. The relational grades linking 9 variables with the collapsibility coefficient, cohesion, and internal friction angle were calculated and ranked (Figure 10). The distinct ranking hierarchies allow understanding which aspect of the mechanical behaviour of loess is influenced by distinct microstructural factors.

Specifically, the macroscopic structural cohesion of loess primarily stems from the compactness of the particle arrangement and the cementing bonds between aggregates. According to the relational grades, dry density exhibits the highest sensitivity to cohesion (0.945), followed by the mesopore area ratio (0.772) and macropore area ratio (0.641). For loess in its original undisturbed state, a higher dry density indicates a tighter packing of the intact structural skeleton, which significantly increases the spatial density of natural cemented contact points (e.g., clay bridges, calcite bonding), thereby providing greater macroscopic cohesion. Most notably, water content (0.628) shows a stronger influence on cohesion than the fractal dimension D_f (0.612). This confirms that moisture variation plays a more direct and relevant role in cohesive degradation than morphological tortuosity. The increase in water content effectively plays a role in reducing matric suction and dissolving the clay bridges and soluble bonds at the contact points, weakening the structural integrity of the soil.

Interestingly, the internal friction angle is governed by a completely distinct micro-mechanism, showing the absolute highest sensitivity to the pore fractal dimension (0.887). Macroscopically, the internal friction angle characterizes sliding friction and mechanical interlocking resistance along the shear failure surface. Microscopically, D_f acts as a crucial geometric parameter quantifying the morphological complexity, boundary roughness, and spatial tortuosity of the pores. During shear deformation, a highly irregular pore boundary forces adjacent soil clusters to undergo more severe rolling, overriding, and rearrangement. This micro-morphological complexity significantly amplifies the interlocking effect between particles. Additionally, dry density (0.841) and the macropore area ratio (0.812) also maintain high relational grades, indicating that the inherent packing density determines the basic sliding friction, while macropores provide the necessary local space for particle rolling and deep interlocking, thereby synergistically influencing the macroscopic shear strength of the soil.

Finally, collapsibility is the most critical factor characterizing the sudden volumetric shrinkage and structural instability of loess upon water infiltration. The GRA results indicate that the macropore area ratio (0.738) is the paramount determinants of collapsibility. The fundamental essence of loess collapsibility lies in the destruction of the metastable, loosely packed skeleton. The macropore fraction intrinsically provides the necessary space for particle displacement during this catastrophic collapse. Furthermore, secondary correlations are observed with dry density (0.674), the mesopore area ratio (0.643) and the pore fractal dimension (0.627). A highly tortuous pore network acts as a complex seepage channel, significantly facilitating the rapid infiltration of moisture. This synergistic interaction between abundant macropore space and complex fractal seepage paths fundamentally accelerates the degradation of the loess structure under hydro-mechanical coupling.

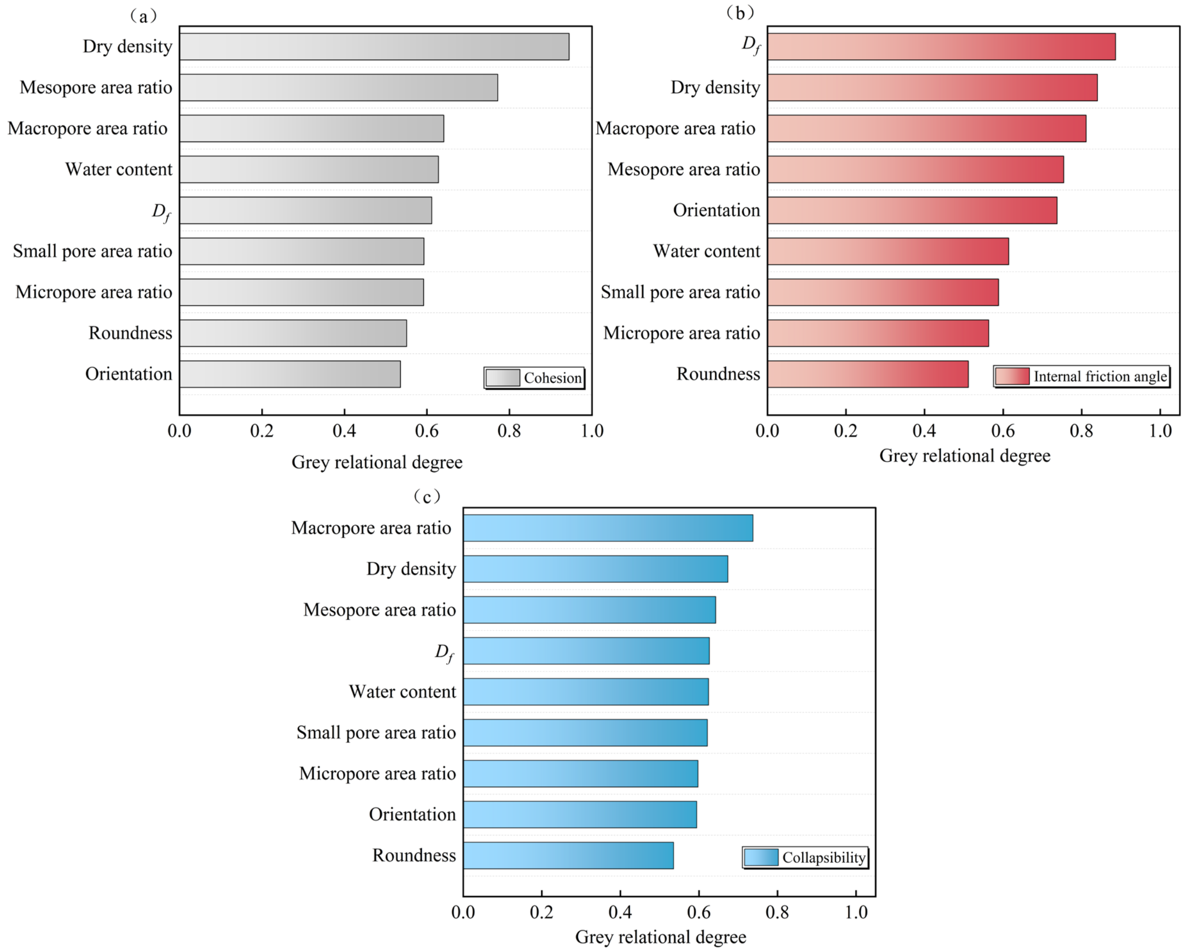

Figure 10. GRA among key factors.

4 Conclusions and future directions

This study quantitatively investigated the spatial heterogeneity of the mechanical properties and microstructural evolution of loess slopes in Yecheng, Xinjiang. By integrating oedometer-collapse tests, direct shear tests, SEM imaging, and GRA, the cross-scale coupling mechanisms between macroscopic behavior and microscopic variables were systematically elucidated. The main conclusions are drawn as follows:

(1) The mechanical behavior and collapsibility of the loess exhibit significant spatial variations from the slope top to the toe. The loess at the upper slope (YC1) acts as an initial tensile stress zone; it demonstrates strong collapsibility (δ_s = 0.076) and lower shear strength, making it highly susceptible to wetting-induced structural instability. Conversely, subjected to substantial passive compressive stress, the loess at the slope toe (YC3) shows enhanced cohesion and internal friction angle, functioning as a terminal retaining block with reduced collapsibility (δ_s = 0.039).

(2) The loess microstructure undergoes a stress-driven, progressive transformation along the slope profile. From YC1 to YC3, the inherently loose, macropore-dominated framework with point contacts degrades into a denser, mesopore/micropore-dominated matrix supported by face contacts and stronger cementation. Driven by sustained shear and overburden stresses, the original vertical orientation of the pores gradually dissipates into sub-horizontal and dispersed configurations. Concurrently, the pores undergo mechanical crushing and fines infilling, leading to an increase in pore roundness and a clear reduction in structural complexity, with the fractal dimension (D_f) decreasing from 1.73 to 1.61.

(3) The GRA model confirms that different macroscopic mechanical parameters are governed by distinct microstructural variables. Cohesion is primarily controlled by dry density, mesopore area ratio, macropore area ratio and water content, which collectively dictate the effective contact and matric suction between soil skeletons. Dry density is expected to mostly acts as a macro-proxy indicating the presence of a spatial concentration of pre-existing natural cementing bonds. The internal friction angle is most sensitive to the pore fractal dimension (D_f), emphasizing that morphological complexity and boundary roughness fundamentally dictate interparticle overriding and interlocking resistance. Ultimately, collapsibility is predominantly determined by the macropore area ratio and dry density, which intrinsically provide the requisite space for structural collapse during water infiltration.

By bridging the gap between localized microstructural deterioration and macroscopic slope failure, this research provides a comprehensive physical understanding of the progressive instability mechanisms in loess slopes. The quantitative findings offer robust theoretical insights for fine-scale landslide hazard assessment and the design of sustainable geotechnical engineering structures in arid environments. Despite these contributions, certain limitations remain. The current study quantified microstructural parameters (D_f) based on 2D SEM images and primarily focused on monotonic hydro-mechanical loading. Because 2D planar projections cannot fully capture the true 3D spatial connectivity of the pore network, further exploration is necessary. Therefore, future research will employ non-destructive 3D imaging techniques (e.g., X-ray CT) to reconstruct genuine 3D pore spaces. Furthermore, the results of XRD analyses, together with SEM and appropriate analysis methods, could provide more insight about the mineralogical context of the specimens.

Data availability statement

The data or datasets that support the findings of this study are available from the corresponding author upon reasonable request.

Declaration of generative AI and AI-assisted technologies

During the preparation of this manuscript, the authors used Grammarly only to improve language and readability in limited sections of the manuscript. Generative AI was not used for data generation, data analysis, interpretation of results, or the development of scientific conclusions. The authors take full responsibility for the content of the manuscript.

Acknowledgments

This study was substantially supported by the National Natural Science Foundation of China (Grant No. 42372320, Grant No. 41972292), the Innovation Capability Support Program of Shaanxi Province (Grant No. 2021TD-54), the Key Research and Development Projects of Shaanxi Province (Grant No. 2022ZDLSF06-03), and the China Postdoctoral Science Foundation Grant No. 2024MD753992).

Authors' contribution

Xuanyu Gao: conceptualization, methodology, investigation, formal analysis, writing—original draft; Wanli Xie: conceptualization, methodology, supervision, funding acquisition, writing—review and editing; Kangze Yuan: investigation; Gabriele Della Vecchia: conceptualization, methodology, supervision, writing—review and editing. All authors have read and agreed to the published version of the manuscript.

Conflicts of interest

The authors declare no conflicts of interest.

References

Bièvre G, Franz M, Larose E, Carrière S, Jongmans D, *et al.* Influence of environmental parameters on the seismic velocity changes in a clayey mudflow (Pont-Bourquin Landslide, Switzerland). *Eng. Geol.* 2018, 245:248–257. DOI: 0.1016/J.ENGGEO.2018.08.013

Chakraborty S, Datta HN, Chakraborty S. Grey relational analysis-based optimization of machining processes: a comprehensive review. *Process Integr. Optim. Sustainability* 2023, 7(4):609–639. DOI: 10.1007/S41660-023-00311-4

Ministry of Housing and Urban-Rural Development of the People's Republic of China. Standard for building construction in collap sible loess regions (GB 50025–2018). 2018. Available: https://ebook.chinabuilding.com.cn/zbooklib/bookpdf/probation?SiteID=1&bookID=113925&utm (accessed on26 December 2018)

Fan X, Xu Q, Scaringi G, Li S, Peng D. A chemo-mechanical insight into the failure mechanism of frequently occurred landslides in the Loess Plateau, Gansu Province, China. *Eng. Geol.* 2017, 228:337–345.DOI: 10.1016/J.ENGGEO.2017.09.003

Gao X, Xie W, Yuan K, Liu Q. Mechanical properties and microstructural evolution of fly ash stabilized loess: insights from multiscale analysis and environmental impacts. *Environ. Technol. Innov.* 2026, 41:04729. DOI: 10.1016/J.ETI.2025.104729

Geertsema M, Highland L, Vaugeouis L. Environmental impact of landslides. In *landslides-disaster risk reduction*, 1st ed. Berlin, Heidelberg: Springer-Verlag, 2009. pp. 589–607.

Griffiths L, Heap MJ, Xu T, Chen C, Baud P. The influence of pore geometry and orientation on the strength and stiffness of porous rock. *J. Struct. Geol.* 2017, 96: 149–160. DOI: 10.1016/J.JSG.2017.02.006

Gao G. Formation and development of the structure of collapsing loess in China. *Eng. Geol.* 1988, 25:235–245. DOI: 10.1016/0013-7952(88)90029-4

Haase D, Fink J, Haase G, Ruske R, Pécsi M, *et al.* Loess in Europe—its spatial distribution based on a European Loess Map, scale 1:2,500,000. *Quat. Sci. Rev.* 2007, 26: 1301–1312. DOI: 10.1016/J.QUASCIREV.2007.02.003

Jia J, Dong Y, Guo X, Liu G, Gu Q. Failure behaviors of terraced loess slope induced by intermittent heavy rainfall: centrifuge model test and numerical simulation. *Front. Earth Sci.* 2025, 13:1696569. DOI: 10.3389/feart.2025.1696569

Juang CH, Dijkstra T, Wasowski J, Meng X. Loess geohazards research in China: advances and challenges for mega engineering projects. *Eng. Geol.* 2019, 251:1–10. DOI: 10.1016/J.ENGGEO.2019.01.019

Kuo Y, Yang T, Huang G. The use of grey relational analysis in solving multiple attribute decision-making problems. *Comput. Ind. Eng.* 2008, 55:80–93. DOI: 10.1016/J.CIE.2007.12.002

Li P, Pan Z, Xiao T, Wang J. Effects of molding water content and compaction degree on the microstructure and permeability of compacted loess. *Acta Geotech.* 2022, 18(2):921–936. DOI: 10.1007/S11440-022-01592-8

Li P, Xie W, Pak RY, Vanapalli SK. Microstructural evolution of loess soils from the Loess Plateau of China. *Catena* 2019, 173:276–288. DOI: 10.1016/J.CATENA.2018.10.006

Lei X. The types of loess pores in China and their relationship with collapsibility. *Sci. China Ser. B* 1988, 31(11):1398–1410. DOI: 10.1360/yb1988-31-11-1398

Li X, Li L. Quantification of the pore structures of Malan loess and the effects on loess permeability and environmental significance, Shaanxi Province, China: an experimental study. *Environ. Earth Sci.* 2017, 76(15):523. DOI: 10.1007/S12665-017-6855-7

Li Y, Shi W, Aydin A, Beroya-Eitner MA, Gao G. Loess genesis and worldwide distribution. *Earth Sci. Rev.* 2020, 201:102947. DOI: 10.1016/J.EARSCIREV.2019.102947

Li Y, Wang Y, Aydin A. Loess structure: evolution and a scale-based classification. *Earth Sci. Rev.* 2024, 249:104665. DOI: 10.1016/J.EARSCIREV.2023.104665

Li Y, Wen B, Aydin A, Ju N. Ring shear tests on slip zone soils of three giant landslides in the Three Gorges Project area. *Eng. Geol.* 2013, 154:106–115. DOI: 10.1016/J.ENGGEO.2012.12.015

Lian B, Peng J, Zhan H, Huang Q, Wang X, *et al.* Formation mechanism analysis of irrigation-induced retrogressive loess landslides. *Catena* 2020, 195:104441. DOI: 10.1016/J.CATENA.2019.104441

Liu S, Yang Y, Cao Y, Xie N. A summary on the research of GRA models. *Grey Syst. Theory Appl.* 2013, 3(1):7–15. DOI: 10.1108/20439371311293651

Liu S, Yang Y, Forrest JY. Grey relational analysis models. In *Grey Systems Analysis*, 1st ed. Singapore: Springer Nature Singapore, 2022. pp. 77–124.

Lv Q, Sui W, Zhang Z, Amat G. Macro–micro correlation analysis on the loess from Ili River Valley subjected to freeze–thaw cycles. *Sci. Rep.* 2024, 14(1):19322. DOI: 10.1038/s41598-024-69868-5

Motameni S, Rostami F, Soroush A, Eslami M. Investigation of soil parameters influencing collapsibility of loess through grey relational analysis. In *Proceedings of the Geotechnical Frontiers 2025,* Louisville, USA, March 2–5, 2025, pp. 555–563.

Nan J, Peng J, Zhu F, Ma P, Liu R, *et al*. Shear behavior and microstructural variation in loess from the Yan'an area, China. *Eng. Geol.* 2021, 280:105964. DOI: 10.1016/J.ENGGEO.2020.105964

Nie Y, Ni W, Lv X, Tuo W, Yuan K. Macroscopic mechanical behavior and microstructural evolution of compacted loess in the Chinese Loess Plateau. *Soil Tillage Res.* 2023, 232:105767. DOI: 10.1016/J.STILL.2023.105767

Peng J, Fan Z, Wu D, Zhuang J, Dai F, *et al.* Heavy rainfall triggered loess–mudstone landslide and subsequent debris flow in Tianshui, China. *Eng. Geol.* 2015, 186:79–90. DOI: 10.1016/J.ENGGEO.2014.08.015

Qin B, Li X, Wang L, Gao R, Chai H. Model interpretation and microscopic characteristics of collapsibility evolution of compacted loess under dry-wet cycles. *Catena* 2024, 246:108413. DOI: 10.1016/J.CATENA.2024.108413

Rabot E, Wiesmeier M, Schlüter S, Vogel HJ. Soil structure as an indicator of soil functions: a review. *Geoderma* 2018, 314:122–137. DOI: 10.1016/J.GEODERMA.2017.11.009

Ministry of Housing and Urban-Rural Development of the People's Republic of China. Standard for geotechnical testing method (GB/T 50123–2019). 2019. Available: https://www.ndls.org.cn/standard/detail/da96a0e4498d42a9f1ab09975af03579 (accessed on 24 May 2019)

Sun Z, Jiang Y, Wang Q, Owens PR. A fractal evaluation of particle size distributions in an eolian loess-paleosol sequence and the linkage with pedogenesis. *Catena* 2018, 165:80–91. DOI: 10.1016/J.CATENA.2018.01.030

Süzen ML, Kaya BŞ. Evaluation of environmental parameters in logistic regression models for landslide susceptibility mapping. *Int. J. Digit. Earth* 2012, 5: 338–355. DOI: 10.1080/17538947.2011.586443

Tang C, Cheng Q, Gong X, Shi B, Inyang HI. Investigation on microstructure evolution of clayey soils: a review focusing on wetting/drying process. *J. Rock Mech. Geotech. Eng.* 2023, 15:269–284. DOI: 10.1016/J.JRMGE.2022.02.004

Vithana SB, Nakamura S, Gibo S, Yoshinaga A, Kimura S. Correlation of large displacement drained shear strength of landslide soils measured by direct shear and ring shear devices. *Landslides* 2011, 9(3):305–314. DOI: 10.1007/S10346-011-0301-9

Wang H, Liao D, Ni W, Yuan K, Guo Y. Shear behavior of intact loess and spatiotemporal evolution of mesoscopic damage: Dynamic identification using CT technology. *J. Rock Mech. Geotech. Eng.* 2025a, 17:7323–7338. DOI: 10.1016/J.JRMGE.2025.01.038

Wang H, Liao D, Ni W, Yuan K, Ren S, *et al*. New insights and modeling of the evolution of loess infiltration characteristics under multiple rainfalls induced by climate on the Loess Plateau of China. *Eng. Geol.* 2025b, 344:107858. DOI: 10.1016/J.ENGGEO.2024.107858

Wang J, Zhang D, Wang N, Gu T. Mechanisms of wetting-induced loess slope failures. *Landslides* 2019, 16(5):937–953. DOI: 10.1007/S10346-019-01144-4

Wang L, Li X, Zheng Z, Zheng H, Ren Y, *et al.* Analysis of the slope failure mechanism a under tunnel erosion environment in the south-eastern Loess Plateau in China. *Catena* 2022, 212:106039. DOI: 10.1016/J.CATENA.2022.106039

Wei Y, Fan W, Yu B, Deng L, Wei T. Characterization and evolution of three-dimensional microstructure of Malan loess. *Catena* 2020, 192:104585. DOI: 10.1016/J.CATENA.2020.104585

Xiao T, Li P, Pan Z, Wang J. Effect of compaction condition on the water retention capacity, microstructure and its evolution during drying of compacted loess. *Geoenviron. Disasters* 2022a, 9(1):27. DOI: 10.1186/S40677-022-00229-Y

Xiao T, Li P, Shao S. Fractal dimension and its variation of intact and compacted loess. *Powder Technol.* 2022b, 395:476–490. DOI: 10.1016/J.POWTEC.2021.09.069

Xiao X, Wang X, Fu K, Zhao Y. Grey relational analysis on factors of the quality of web service. *Phys. Procedia* 2012, 33:1992–1998. DOI: 10.1016/J.PHPRO.2012.05.313

Xie W, Guo Q, Wu J, Li P, Yang H, *et al.* Analysis of loess landslide mechanism and numerical simulation stabilization on the Loess Plateau in Central China. *Nat. Hazard.* 2021, 106(1):805–827. DOI: 10.1007/S11069-020-04492-W

Xu L, Coop M, Zhang M, Wang G. The mechanics of a saturated silty loess and implications for landslides. *Eng. Geol.* 2018, 236:29–42. DOI: 10.1016/J.ENGGEO.2017.02.021

Xu P, Qian H, Chen J, Wang L, Abliz X, *et al.* New insights into microstructure evolution mechanism of compacted loess and its engineering implications. *Bull. Eng. Geol. Environ.* 2023, 82(1):36. DOI: 10.1007/S10064-022-03058-3

Ye S, Huang A, Zhu Y. Slope stability prediction using grey entropy correlation analysis. *Soil Mech. Found. Eng.* 2024, 61(5):419–425. DOI: 10.1007/S11204-024-09992-6

Yuan K, Ni W, Lv X, Zhu M, Wang H, *et al.* Mechanical properties and microstructure evolution of Malan loess. *Quat. Int.* 2022, 637:74–84. DOI: 10.1016/J.QUAINT.2022.06.008

Zhang F, Wang G. Effect of irrigation-induced densification on the post-failure behavior of loess flowslides occurring on the Heifangtai area, Gansu, China. *Eng. Geol.* 2018 ,236:111–118. DOI: 10.1016/J.ENGGEO.2017.07.010

Zhang M, Liu J. Controlling factors of loess landslides in western China. *Environ. Earth Sci.* 2010, 59:1671–1680. DOI: 10.1007/S12665-009-0149-7/FIGURES/12

Zhang M, Yin Y. Dynamics, mobility-controlling factors and transport mechanisms of rapid lon g-runout rock avalanches in China. *Eng. Geol.* 2013, 167:37–58. DOI: 10.1016/J.ENGGEO.2013.10.010

Zhang Y, Chen Y. Research trends and areas of focus on the Chinese Loess Plateau: a bibliometric analysis during 1991–2018. *Catena* 2020, 194:104798. DOI: 10.1016/J.CATENA.2020.104798

Zheng H, Powell CMA, Butcher K, Cao J. Late Neogene loess deposition in southern Tarim Basin: tectonic and palaeoenvironmental implications. *Tectonophysics* 2003, 375:49–59. DOI: 10.1016/S0040-1951(03)00333-0

Zhou Y, Yu B, Fan W, Dijkstra T, Wei Y, *et al.* 3D characterization of localized shear failure in loess subject to triaxial loading. *Eng. Geol.* 2023, 322:107174. DOI: 10.1016/J.ENGGEO.2023.107174

Zhuang J, Cui P, Wang G, Chen X, Iqbal J, *et al.* Rainfall thresholds for the occurrence of debris flows in the Jiangjia Gully, Yunnan Province, China. *Eng. Geol.* 2015, 195:335–346. DOI: 10.1016/J.ENGGEO.2015.06.006

Zhuang J, Peng J, Wang G, Javed I, Wang Y, *et al.* Distribution and characteristics of landslide in loess plateau: a case study in Shaanxi province. *Eng. Geol.* 2018, 236:89–96. DOI: 10.1016/J.ENGGEO.2017.03.00